

# Grains in Selectively Grown MoS<sub>2</sub> Thin Films

Hyung-Jun Kim, Hojoong Kim, Suk Yang, and Jang-Yeon Kwon\*

Transition metal dichalcogenides (TMDCs) have recently been studied using various synthesis methods, such as chemical vapor deposition for large-scale production. Despite the realization of large-scale production with high material quality, a range of approaches have been made to solve the patterning issue of TMDCs focusing on the application of integrated devices; however, patterning is still under study to accurately represent nanoscale-sized patterns, as well as the desired positions and shapes. Here, an insulating substrate is treated selectively with O<sub>2</sub> plasma, and MoS<sub>2</sub> growth is induced in the superhydrophilic area. Selectively well-grown MoS<sub>2</sub> patterns are confirmed by atomic force microscopy and Raman and photoluminescence spectroscopy. In addition, the grain size, according to the growth size, and grain boundary are analyzed by annual dark field transmission electron microscopy (TEM) and spherical aberration-corrected scanning TEM to confirm the selective growth. An analysis of the device performance and the optical properties reveals an enhancement with increasing grain size. This method presents the path of the growth technique for patterning, as well as the direction that can be applied to devices and integrated circuits.

Transition metal dichalcogenides (TMDCs) have been actively studied because of their excellent semiconducting and optical properties despite the thinness of the three-atom-thick, 2D structure. TMDCs have attracted considerable attention for large areas using chemical synthesis methods, such as chemical vapor deposition (CVD),<sup>[1–3]</sup> physical vapor deposition,<sup>[4,5]</sup> and atomic layer deposition (ALD).<sup>[6–8]</sup> These materials have various applications, such as memory devices,<sup>[9–11]</sup> photo sensors,<sup>[12–14]</sup> and field-effect transistor (FET) devices.<sup>[15,16]</sup> On the other hand, there is a lack of research on the patterning of large area TMDCs for the desired size, modifiable shape, and the application of integrated circuits.

Unlike patterning methods of graphene materials, which are currently reported in various ways, such as chemical and physical patterning,<sup>[17,18]</sup> studies of patterning TMDC have been reported, including the methods of stamping,<sup>[19,20]</sup> patterned MoO<sub>3</sub>, WO<sub>3</sub> sulfurization,<sup>[21,22]</sup> etc. Although these methods are important for patterning TMDCs, their properties

are limited due to the presence of residue. As an alternative to the above problems, a few groups have studied the lithography-free process.<sup>[23]</sup> TMDCs by chemical synthesis using two powders are affected by the change in surface energy on insulator. On the other hand, it has been reported that the electrical properties are inferior to those of MoS<sub>2</sub> grown by general CVD, making it necessary to improve the electrical properties through the atomic scale analysis of patterned MoS<sub>2</sub>. Characterization of the grain on the atomic scale is a typical example of the research to improve the material properties, such as the electrical and mechanical properties of materials.

An analysis of the grain structure of 2D materials, such as synthesized graphene and TMDCs, on the atomic scale is very important for understanding and controlling the defective few-layer material properties. As electrical and mechanical

properties of 2D materials differ according to the grain structure and size, as reported previously,<sup>[24]</sup> control of the grain properties can make a significant contribution to improving its material properties. Grains of 2D materials, such as graphene, can vary in size depending on the growth conditions, such as the gas concentration,<sup>[25]</sup> and growth time,<sup>[26]</sup> as previously reported. TMDCs have also been studied for the characterization of grains and grain boundaries, and the mechanism of the grain boundary characterization of MoS<sub>2</sub> has been reported.<sup>[27]</sup> Nevertheless, there has been much less study on the grains of MoS<sub>2</sub> grown as a function of the surface energy.

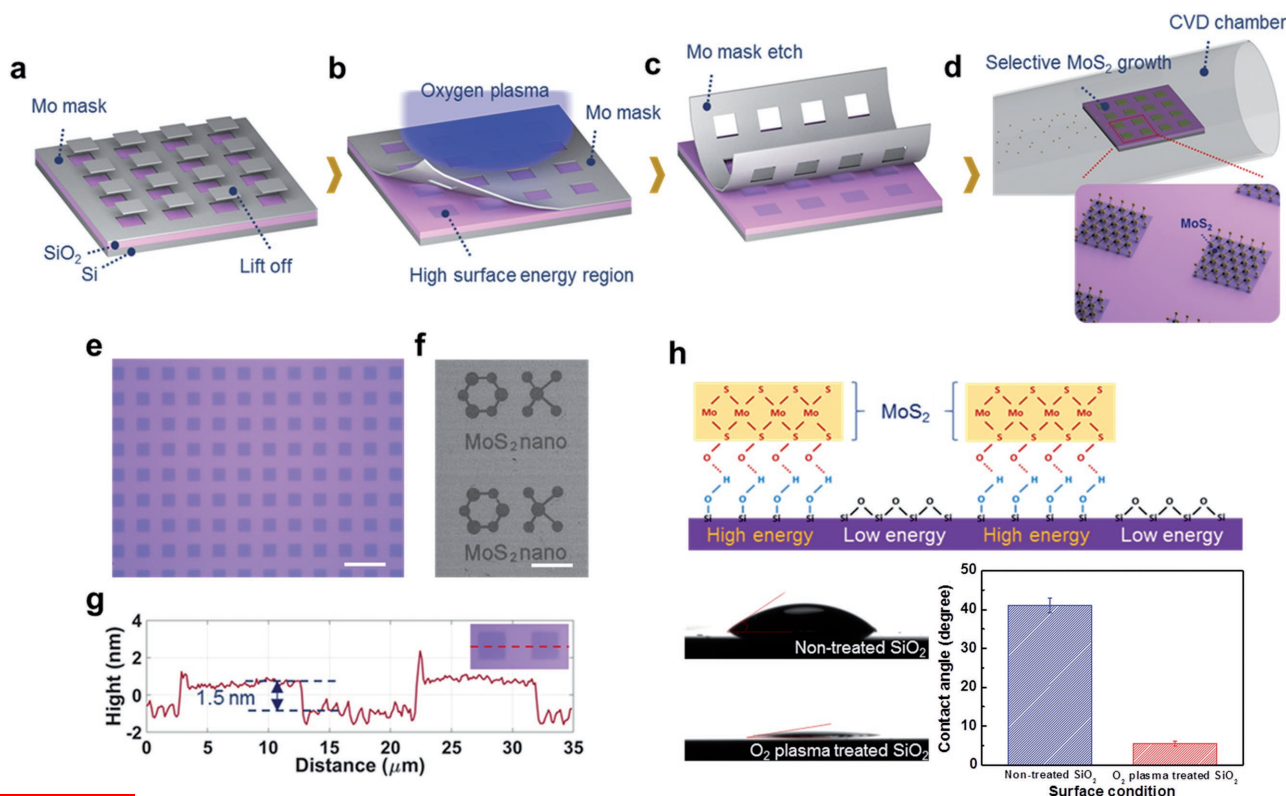
This Communication reports the selectively grown MoS<sub>2</sub> by partially treating the surface energy using O<sub>2</sub> plasma through a new patterning procedure, and the electrical characteristics of MoS<sub>2</sub> were analyzed through grains of MoS<sub>2</sub> depending on the growth size.

Figure 1a–d presents the process of selective growth MoS<sub>2</sub>. Molybdenum (Mo) was deposited completely on SiO<sub>2</sub>/Si to form a mask using maskless-lithography technology (Figure 1a). This is because the shadow effect causes an unwanted growth pattern when using an existing shadow mask (Figure S1, Supporting Information); the metal itself is used for mask application. A selective surface treatment was performed by applying oxygen plasma to the area where the Mo was lifted off (Figure 1b). The Mo mask was fully etched with wet-etchant (Figure 1c), and reacted with MoO<sub>3</sub> and S by CVD to selectively grow MoS<sub>2</sub> on the surface with high surface energy, as shown in Figure 1d (see the Experimental Section). Figure 1e presents

H.-J. Kim, H. Kim, S. Yang, Prof. J.-Y. Kwon  
 School of Integrated Technology  
 Yonsei University  
 Yeonsu-gu, Incheon 21983, Republic of Korea  
 E-mail: jangyeon@yonsei.ac.kr

H.-J. Kim, H. Kim, S. Yang, Prof. J.-Y. Kwon  
 Yonsei Institute of Convergence Technology  
 Yeonsu-gu, Incheon 21983, Republic of Korea

DOI: 10.1002/sml.201702256



**Figure 1.** a–d) Schematic outline of the MoS<sub>2</sub> growth patterning procedure. e) Patterned arrays of the grown MoS<sub>2</sub> (OM image; grown MoS<sub>2</sub> size  $10 \times 10 \mu\text{m}^2$ , the scale bar is  $33 \mu\text{m}$ ). f) Desired shapes of the grown MoS<sub>2</sub> (HR-SEM image; shapes of “MoS<sub>2</sub> nano,” the scale bar is  $80 \mu\text{m}$ ). g) The thickness of the selectively grown MoS<sub>2</sub> layer is 1.5 nm from the AFM height profile along the red line shown in the inset. The inset shows the selectively grown MoS<sub>2</sub> of  $10 \times 10 \mu\text{m}^2$  size. h) Schematic illustration of the mechanism of selective surface treatment by O<sub>2</sub> plasma. The water contact angles on SiO<sub>2</sub> of the nontreated and O<sub>2</sub> plasma-treated area measured are shown with the statistical plot below the schematic image.

an optical microscopy (OM) image of the selectively grown MoS<sub>2</sub>, which shows that MoS<sub>2</sub> is grown in the desired area with a patterned size of  $10 \times 10 \mu\text{m}^2$ . High-resolution-scanning electron microscopy (HR-SEM) (Figure S2a,b, Supporting Information) showed that MoS<sub>2</sub> had grown well in the desired area. Cross-sectional measurements using focused ion beam (FIB) confirmed that MoS<sub>2</sub> had grown in the mono to double layers (Figure S2c, Supporting Information), and the presence of Mo and S in scanning transmission electron microscopy-energy dispersive X-ray spectrometer (STEM-EDS) maps showed that MoS<sub>2</sub> had been synthesized. To confirm that MoS<sub>2</sub> can be synthesized in various shapes by these properties, it was synthesized with the pattern of a geometric shape and word (“MoS<sub>2</sub> nano” pattern), as shown in the HR-SEM image in Figure 1f. In addition, the atomic force microscopy (AFM) height profile of the red line in the inset revealed an MoS<sub>2</sub> thickness of  $\approx 1.5 \text{ nm}$ , which is around two layers (Figure 1g). Figure 1h shows the growth mechanism of MoS<sub>2</sub> according to the surface energy. When O<sub>2</sub> plasma is applied, Si bonds are broken by plasma, and O and H bonds to some dangling bonds. Owing to the dangling bonds, the imbalance of surface bonding increases the surface energy. These theories are well known, but simple patterns and theories can lead to selective MoS<sub>2</sub> patterns. The contact angle was severally measured to confirm the difference in surface energy (Figure S3a–l, Supporting Information). The difference

in contact angle with the O<sub>2</sub> plasma treatment time was identified to determine the conditions when the surface energy is maximized. As shown in Figure S3m (Supporting Information), the contact angle was minimized at 600 s of O<sub>2</sub> plasma treatment time, and the measured degree was  $5.6^\circ \pm 0.7^\circ$ , which confirmed the maximum point of the surface energy. In addition, the desired pattern was clearly visible at 600 s of selective growth under the conditions shown in Figure S3n (Supporting Information).

Raman and photoluminescence (PL) spectroscopy were conducted on bulk and selectively grown MoS<sub>2</sub> using a typical 532 nm laser (Figure 2). The Raman peaks for the selectively grown MoS<sub>2</sub> peaks corresponded to those of the normal bulk samples (Figure 2a). On the other hand, the difference in frequency ( $\Delta$ ) between  $E_{2g}^1$  and  $A_{1g}$  was  $\approx 21 \text{ cm}^{-1}$  for the selective sample and  $23 \text{ cm}^{-1}$  for the bulk sample, with peaks becoming narrower for both. The changes in the peaks for  $A_{1g}$  and  $E_{2g}^1$  can be explained by the strong interlayer interaction and Coulombic screening effect, which is a stronger restoring interaction acting on the atoms with an increase in the number of short-range and long-range interactions.<sup>[28–30]</sup> The Raman mapping images show the peak intensities of MoS<sub>2</sub>, with the  $E_{2g}^1$  and  $A_{1g}$  presented in the inset of Figure 2a. The Raman mapping results showed that selectively grown MoS<sub>2</sub> is grown uniformly. The X-ray photoelectron spectroscopy (XPS) spectra for the Mo 3d and S 2p peak indicated a

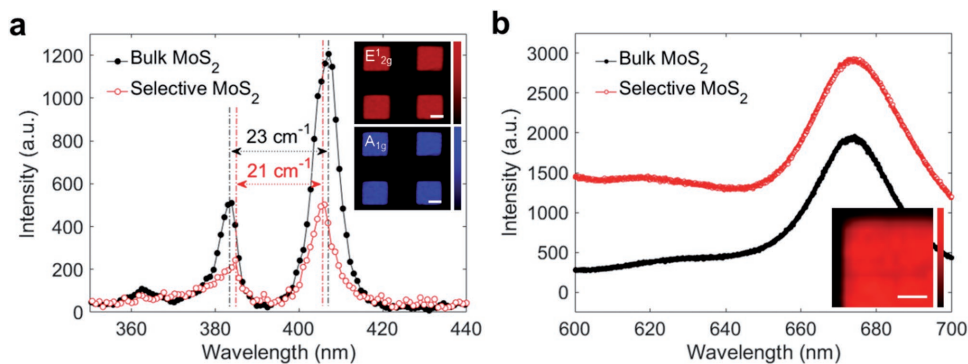


**Figure 2.** a) Typical 532 nm laser Raman spectra of bulk and selective MoS<sub>2</sub>. The inset shows the Raman mapping images of E<sub>1g</sub> and A<sub>1g</sub> peak intensities of selective MoS<sub>2</sub>. The scale bar is 5  $\mu$ m. b) Typical 532 nm laser PL spectra from bulk and selective MoS<sub>2</sub>. The inset shows the PL mapping images of selective MoS<sub>2</sub> at 677 nm. The scale bar is 3  $\mu$ m.

stoichiometric ratio of 1.0:1.9 (Mo:S) for the synthesized MoS<sub>2</sub>, which is in agreement with previous results (Figure S4a–d, Supporting Information).<sup>[31]</sup> The TEM-EDS data for Mo and S elements also indicated an averaged element ratio of 1.0:2.0 (Mo:S), suggesting the structure is close to MoS<sub>2</sub> (Figure S4e,f, Supporting Information). The PL properties of the synthesized sample indicated a drastic emission of photon energy at the two peaks at  $\approx$ 625 and 677 nm when compared to the bulk sample (Figure 2b). The PL mapping images revealed the peak intensities of the synthesized MoS<sub>2</sub> at 677 nm as shown in the inset of Figure 2b. The high intensity PL peaks with the synthesized MoS<sub>2</sub> were assigned to the band gap transition from direct to indirect compared to bulk MoS<sub>2</sub>, which is consistent with the previously reported band gap of synthesized low layer MoS<sub>2</sub>.<sup>[32,33]</sup>

Figure 3a presents an OM image of the synthesized MoS<sub>2</sub> when 0.1 mg of MoS<sub>2</sub> powder was used. The synthesis of MoS<sub>2</sub> is not performed properly, which was confirmed by the Raman mapping image in Figure 3b. As shown in Figure 3c, no peaks corresponding to MoS<sub>2</sub> were observed in the selectively treated area, which is indicated as a red box in Figure 3a, and there was no difference compared to the nonselective treated areas. On the other hand, when the amount of the powder was increased to 0.5 mg, a square-shaped MoS<sub>2</sub> could be identified, as shown in Figure 3d. This was confirmed by the Raman mapping image of Figure 3e. In Figure 3f, a clear peak for MoS<sub>2</sub> was observed in the selectively treated area, pointing to a red box in Figure 3d. A clear difference in the peaks can be identified when compared with the nonselective treated areas. When the amount of MoO<sub>3</sub> powder was increased by 1 mg, MoS<sub>2</sub> is entirely deposited (Figure 3g,h). In addition, the peaks were observed in both the selectively treated area and the non-selective treated area, and the pattern could not be identified (Figure 3i). Therefore, the selective MoS<sub>2</sub> pattern was possible by optimizing the amount of main MoO<sub>3</sub> powder, and that MoS<sub>2</sub> can be synthesized in a desired position and shape in a complicated circuit and structure.

To selectively synthesize MoS<sub>2</sub>, the amount of MoO<sub>3</sub> powder was much lower than that of sulfur powder. Generally, to grow an ideal MoS<sub>2</sub> with a conventional triangular shape, the MoO<sub>3</sub>:S ratio of each powder was  $\approx$ 1:100 in powder synthesis. On the other hand, it is necessary to synthesize it at a powder ratio of  $\approx$ 1:1000 for the selective synthesis. Owing to the relatively small

amount of reactance, the material properties of MoS<sub>2</sub> may be degraded. This may result in lower electrical and mechanical efficiency due to the relatively small grain size. This is expected to be solved by adjusting the growth time, pressure, and the control of nucleation site in future works. MoS<sub>2</sub> growth is sensitive to the energy of the surface in terms of the surface on the substrate. In addition, a limited treatment for controlling the surface energy can affect the growth of MoS<sub>2</sub> through the seeds depending on the treated area. The principle of material growth and characteristics can be confirmed by changing the growth nature according to the size of artificially grown MoS<sub>2</sub>. Traditionally, the mechanism of grain characterization through material growth is that the grain size increases with decreasing amount of seed in the same area, and when the seed grows from the edge, the grain size increases gradually with time. Based on the optimized condition of selective growth, the grain size was observed by increasing the size of the pattern from  $10 \times 10 \mu\text{m}^2$  to  $50 \times 50 \mu\text{m}^2$  to identify the mechanism of the grains by selective growth. Each pattern was transferred to a TEM grid using poly(methyl methacrylate) (PMMA; Figure S5, Supporting Information; see the Experimental Section).

To determine the grain size according to the pattern size of MoS<sub>2</sub>, an image was obtained by annual dark field TEM (ADF-TEM), the selected area diffraction (SAED) pattern of the image was analyzed, and an image of the grains was obtained through simulation. Figure 4a shows an OM image of  $10 \times 10 \mu\text{m}^2$  grown MoS<sub>2</sub>. The ADF-TEM image was obtained based on the pattern of  $10 \times 10 \mu\text{m}^2$  (Figure 4b) with the SAED pattern image (Figure 4c). The SAED pattern was formed by sixfold symmetry, and three spots were selected to perform the grain simulation. In the grain simulation, the spot corresponding to the SAED pattern was assigned to the red, green, and blue (RGB) color, respectively, to obtain an image, as shown in Figure 4d. As shown in Figure 4e, the grain size was prominent at 10–20 nm. Figure 4f–i presents the results of grain size analysis of  $50 \times 50 \mu\text{m}^2$  patterned MoS<sub>2</sub>, which is the same as the method used for  $10 \times 10 \mu\text{m}^2$  patterned MoS<sub>2</sub> analysis. As shown in Figure 4j, the grain size ranged from 40 to 50 nm. In addition, no noticeable change of the grain size was observed at less than  $10 \times 10 \mu\text{m}^2$  pattern (Figure S6, Supporting Information). In the case of  $100 \times 100 \mu\text{m}^2$  pattern, the grain sizes were  $\approx$ 10 nm larger than the result of  $50 \times 50 \mu\text{m}^2$  pattern. Through



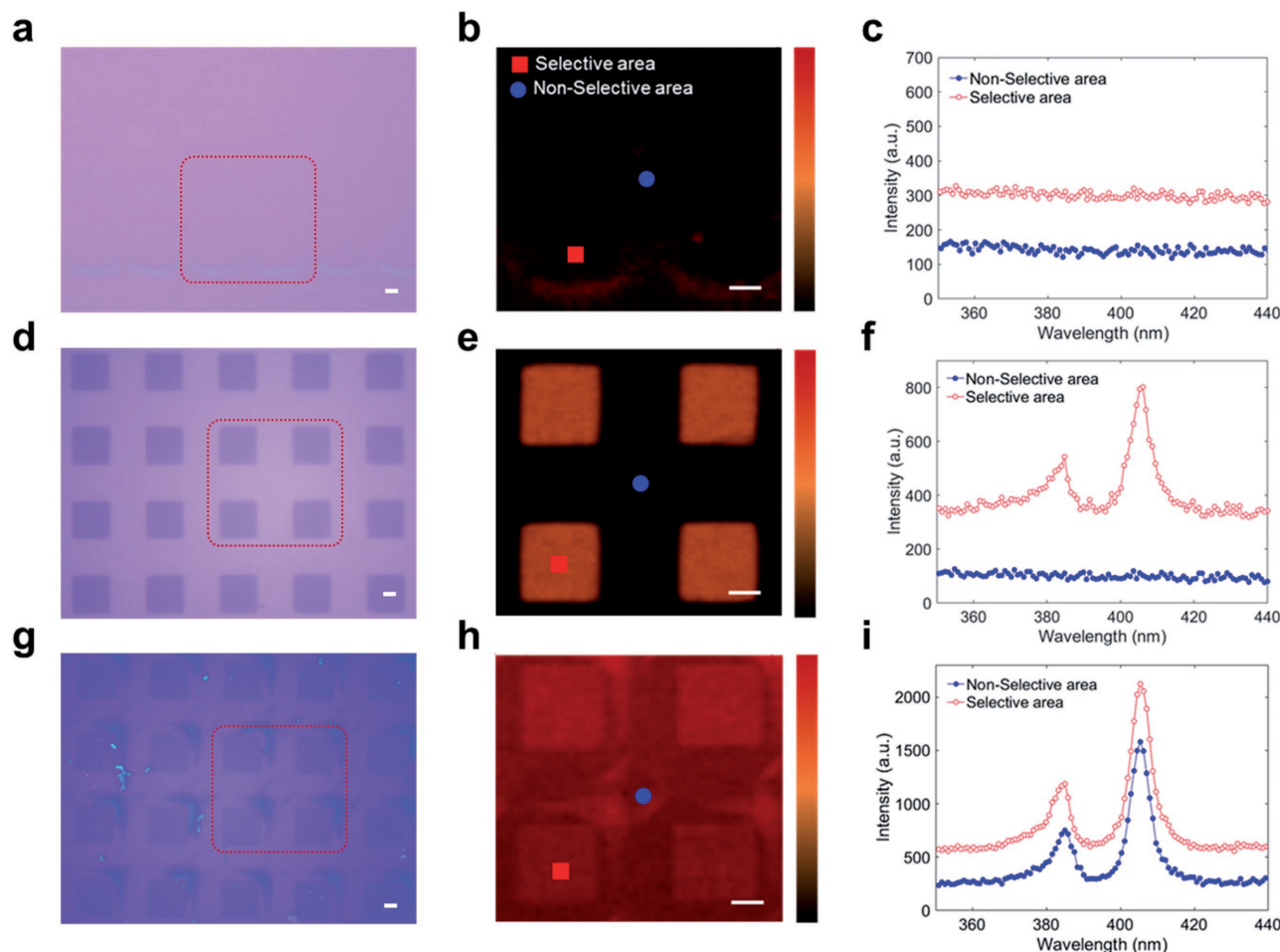


**Figure 3.** Optimization of the selective growth conditions with changing quantities of the  $\text{MoO}_3$  powder. a) The OM image of the grown  $\text{MoS}_2$  using 0.1 mg of  $\text{MoO}_3$  powder. The scale bar is 3.5  $\mu\text{m}$ . b) Raman mapping images of the red dot square in (a). The scale bar is 4  $\mu\text{m}$ . c) Raman spectra of the red square of selectively grown  $\text{MoS}_2$  and blue circle of nongrown area. d) OM image of the grown  $\text{MoS}_2$  using 0.5 mg of  $\text{MoO}_3$  powder quantities. e) Raman mapping images of the red dot square in (d). f) Raman spectra of the red square of selectively grown  $\text{MoS}_2$  and the blue circle of the nongrown area. g) OM image of the grown  $\text{MoS}_2$  using 1 mg of  $\text{MoO}_3$  powder. h) Raman mapping images of red dot square in (g). i) Raman spectra of red square of selectively grown  $\text{MoS}_2$  and blue circle of nongrown area.

the various pattern sizes, we confirmed that the lower limit of the grain size was around 10 nm and the upper limit of the grain size was around 80 nm (Figure S7, Supporting Information). Hence, the grain size increased with increasing pattern size of  $\text{MoS}_2$ , which indicates that the treated size affected the growth of  $\text{MoS}_2$ . As described above, the difference in grain size per size of the  $\text{O}_2$  plasma-treated region can be explained as follows. In the  $10 \times 10 \mu\text{m}^2$  treated region, seeds of  $\text{MoS}_2$  are generated from the boundary where a difference in surface energy appears, and growth starts inward depending on the seed (Figure S8a–c, Supporting Information). On the other hand, in the treated region of  $50 \times 50 \mu\text{m}^2$ , the seed grows from the boundary of the surface energy like the treated region of  $10 \times 10 \mu\text{m}^2$ , but the grain size can become larger because the treated region is relatively wide (Figure S8d,e, Supporting Information).<sup>[34]</sup> Therefore, the grain size of the central part of the treated area of  $50 \times 50 \mu\text{m}^2$  is larger than that of  $10 \times 10 \mu\text{m}^2$  (Figure S8f,g, Supporting Information). During the growth process, the point where the grains meet each other forms a

boundary, establishing two or three planes, and the shape is formed at a constant angle in a zigzag pattern, as reported previously (Figure S9, Supporting Information).<sup>[35,36]</sup>

To evaluate the electronic characteristics of the selectively grown  $\text{MoS}_2$  layer of  $10 \times 10 \mu\text{m}^2$  and  $50 \times 50 \mu\text{m}^2$  sizes, we fabricated bottom-gated FET on 300 nm thick  $\text{SiO}_2$  thermally grown on a highly doped p-type Si wafer. Mo (150 nm) was deposited via DC sputter to be used as source and drain electrodes and patterned via a conventional liftoff process with 30 nm  $\text{Al}_2\text{O}_3$  capping layer. (Figure 5a,b). Figure 5c demonstrates the output curve for an FET fabricated with  $10 \times 10 \mu\text{m}^2$  and  $50 \times 50 \mu\text{m}^2$  grown  $\text{MoS}_2$  FETs with gating voltages ( $V_g$ ) from 0 to 100 V at an interval of 10 V. With an increase in drain voltage ( $V_d$ ), the values for the drain current ( $I_d$ ) of the  $\text{MoS}_2$  FETs of  $50 \times 50 \mu\text{m}^2$  size increased over six times that of  $\text{MoS}_2$  FETs of  $10 \times 10 \mu\text{m}^2$  grown size. We also measured the transfer curves of the  $\text{MoS}_2$  FET of  $10 \times 10 \mu\text{m}^2$  and  $50 \times 50 \mu\text{m}^2$  sizes (Figure 5d), and the field-effect mobility was calculated as  $[dI_{ds}/dV_g] \cdot [L/(WC_iV_{ds})]$ , where  $L$  and  $W$  are the length and width of

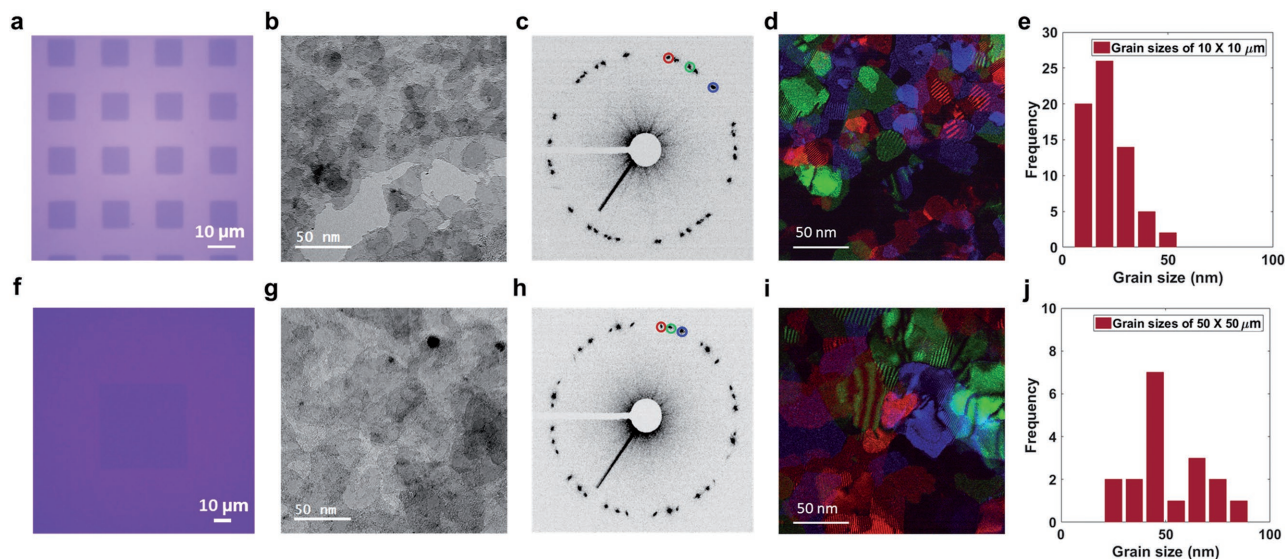


**Figure 4.** Grain analysis with increasing size of the MoS<sub>2</sub> growth pattern. a) OM image of 10 × 10 μm<sup>2</sup> size of the MoS<sub>2</sub> growth pattern. b) Bright-field TEM image in (a). c) SAED pattern acquired from the total area in (b), showing three points of sixfold symmetry diffraction patterns. d) False-color mapped dark-field TEM image using the three-color spots marked in (c). e) Histogram of the grain size, yielding a grain size of 17.5 nm. f) The OM image of a 50 × 50 μm<sup>2</sup> size of the MoS<sub>2</sub> growth pattern. g) Bright-field TEM image in (f). h) SAED pattern acquired from the total area in (g), showing three points of sixfold symmetry in the diffraction patterns. i) False-color mapped dark-field TEM image using the three-color spots marked in (h). j) Histogram of the grain size, yielding a grain size of 45 nm.

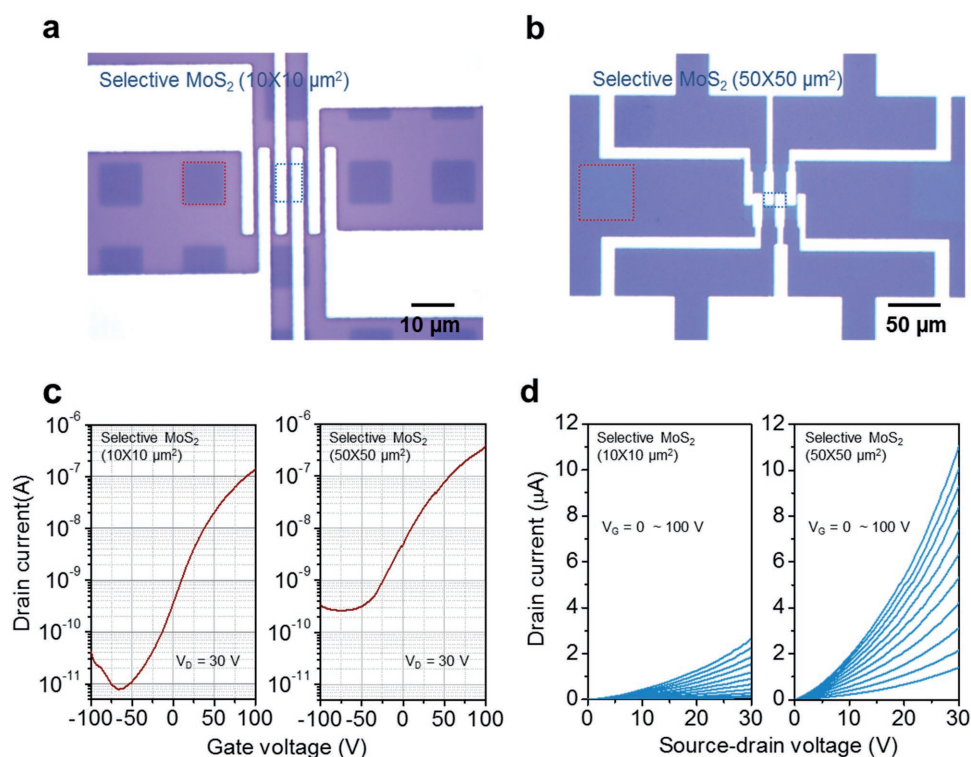


**Figure 5.** Electrical properties with increasing size of the MoS<sub>2</sub> growth pattern. a) OM image of 10 × 10 μm<sup>2</sup> array. The inset is the OM image of the fabricated MoS<sub>2</sub> FET device, and the scale bar is 10 μm. b) OM image of 50 × 50 μm<sup>2</sup> array. The inset shows an OM image of the fabricated MoS<sub>2</sub> FET device, and the scale bar is 50 μm. c) Output characteristics with gating voltages (V<sub>gs</sub>) ranging from 0 to 100 V with respect to the 10 V interval. The left and right-side slopes are 10 × 10 μm<sup>2</sup> and 50 × 50 μm<sup>2</sup> growth size MoS<sub>2</sub>-FET, respectively. d) Transfer characteristics of the MoS<sub>2</sub> FETs measured with a source drain bias (V<sub>ds</sub>) of 30 V. The left and right-side slopes are 10 × 10 μm<sup>2</sup> and 50 × 50 μm<sup>2</sup> growth size MoS<sub>2</sub> FET, respectively.

the channel,  $C_i$  is the capacitance of the gating oxide, and  $V_g$  is the bias that was applied to the back gate. Both MoS<sub>2</sub> FET samples are fixed width and length rate. These results show that the mobility increased by about 2.5 times from 0.044 to 0.116 cm<sup>2</sup> V<sup>-1</sup> s<sup>-1</sup> after increasing the MoS<sub>2</sub> grown size. According to the above results, as the grown size of MoS<sub>2</sub> increases, the grain size increases and the mobility increases as well. It can be explained that carrier scattering occurs in the grain boundary and the grain boundary decreases as the grain size increases, so carrier scattering decreases. This leads to an increase in mobility. On the other hand, as grain size decreases, carrier scattering increases and mobility decreases. Several studies have shown that the grain boundaries of 2D materials, such as graphene and TMDCs, can degrade the device properties.<sup>[24]</sup> In the present study, when  $W$  of an FET is increased in accordance with the size of MoS<sub>2</sub>, the field-effect mobility of the FETs is reduced from 0.003 cm<sup>2</sup> V<sup>-1</sup> s<sup>-1</sup> in 50 × 50 μm<sup>2</sup> to 0.044 cm<sup>2</sup> V<sup>-1</sup> s<sup>-1</sup> in 10 × 10 μm<sup>2</sup> (Figure S10a–d, Supporting Information). Although the grain size for 50 × 50 μm<sup>2</sup> size of MoS<sub>2</sub> flakes is larger than that for 10 × 10 μm<sup>2</sup> size flakes, the field-effect mobility of the FETs made from the former is lower than that of the FETs made from the latter.

Besides the electronic properties, we measured optical properties to identify the other possible size effects of the MoS<sub>2</sub> grains. Raman and PL of 10 and 50 μm patterns were measured to confirm the optical properties of the material as shown in Figure S11 (Supporting Information). The intensity of the Raman peak resulted in the fact that the peak of the 50 μm pattern was slightly lower than that of the 10 μm pattern (Figure S11a, Supporting Information). However, PL peak shows that the intensity of the peak of the 50 μm pattern is more than four times higher than that of the 10 μm pattern (Figure S11b, Supporting Information). It can be concluded that as the sizes of MoS<sub>2</sub> pattern were increased, the grain sizes were increased, and the number of grain boundaries was decreased; it causes enhancement of the PL intensity. The grain boundaries have a negative effect on electron transport and optical properties.<sup>[37]</sup> Therefore, through further identification based on its growth mechanism, it will be necessary to achieve a steady high performance in patterned TMDC-based devices. To this end, various researchers have attempted to reduce the number of grain boundaries, which is a fatal disadvantage of a 2D material grown by CVD, and various growth techniques should be attempted to reduce the number of grain boundaries.

This Communication reported selective growth as a method for MoS<sub>2</sub> patterning that can enable growth in a desired area, tunable growth size, and various growth shapes. Raman and PL spectroscopy showed that the MoS<sub>2</sub> films were grown selectively on the O<sub>2</sub> plasma treated surface. Through a change in the growth size of MoS<sub>2</sub>, the grain size and its growth mechanism were identified by ADF-TEM. An analysis of the electrical and optical properties also showed an increase with increasing growth size, indicating that the grain size of the selectively grown MoS<sub>2</sub> contributed to the enhanced properties of the MoS<sub>2</sub> materials.

## Experimental Section

**Growth Procedure:** Mo was deposited on SiO<sub>2</sub>/Si to form a mask using maskless-lithography technology. A selective surface treatment was

performed by applying O<sub>2</sub> plasma to the area where Mo was lifted off. The Mo mask was fully etched with a wet-etchant (DI:NH<sub>4</sub>OH:H<sub>2</sub>O<sub>2</sub> = 70:30:5), and reacted with MoO<sub>3</sub> and S by CVD to selectively grow MoS<sub>2</sub> on the surface with high surface energy (0 and 600 s treatment times). The selectively grown MoS<sub>2</sub> was synthesized in a multizone furnace (SNTEK) equipped with a 1 in. diameter quartz tube, as shown in Figure 1a. MoO<sub>3</sub> powder (Sigma-Aldrich, 0.1, 0.5, and 1 mg) and S powder (Sigma-Aldrich, 350 mg) were placed successfully on the Al<sub>2</sub>O<sub>3</sub>-coated boats in each hot center. A 300 nm thick SiO<sub>2</sub> layer was grown thermally on a highly doped p-type Si wafer and placed face down on the boat in the middle of the zone. The MoO<sub>3</sub> and S vapors were transported using ultrahigh purity Ar (99.999%) carrier gas. The pressure of the quartz tube remained at 1 Torr of Ar. The growth method is as follows. The quartz tube was kept for 1 h at 150 °C with 500 sccm to remove any organic contaminations on the surface. The furnace was ramped to 840 °C at 14 °C min<sup>-1</sup> with 30 sccm for the second zone (MoO<sub>3</sub>), rest for 10 min at 840 °C, 146 °C at 4.3 °C min<sup>-1</sup> with 30 sccm for third zone (S). Finally, the furnace was opened and 500 sccm was flowed for rapid cooling.

**Preparation of the Plane View TEM Samples:** Two types of TEM grid samples were prepared. First, the selectively grown MoS<sub>2</sub> was transferred to the TEM grid to view the plane of the MoS<sub>2</sub> as follows.<sup>[38]</sup> The SiO<sub>2</sub>/Si substrate with the selectively grown MoS<sub>2</sub> samples was first spin-coated with PMMA (transparent thermoplastic) (A4, 4 wt% dissolved in ethyl lactate) at 3000 rpm for 60 s and then dried in air at 120 °C for 5 min. The PMMA/MoS<sub>2</sub>/SiO<sub>2</sub> substrates were immersed in a warm potassium hydroxide (KOH, Si etchant) solution (1 mol L<sup>-1</sup>) to etch away the SiO<sub>2</sub> layers. The floating PMMA film was carefully picked up, washed thoroughly in deionized (DI) water, and dried naturally in a silica gel environment. The PMMA film was lifted out using a lacey carbon film-coated TEM grid. The PMMA film on the TEM grid was removed with warm acetone (50 °C) overnight, rinsed with isopropyl alcohol (substrate cleaning purposes), and dried with flowing Ar.

**Optical Characterization:** Raman and PL spectroscopy were carried out using a Horiba Aramis LabRAM. The excitation energy of the laser was 532 nm with an estimated laser spot size of 1 μm; the Si peak at 520 cm<sup>-1</sup> was used for calibration. Raman mapping results were obtained with a ×100 scale objective, 600 grooves per millimeter grating, and a 0.5 μm step. The thickness and surface morphology of the MoS<sub>2</sub> were characterized by AFM (Park Systems), SEM (JEOL), and OM (LV100D, Nikon). The grain and nanostructure of the MoS<sub>2</sub> were characterized by ADF-TEM (JEM-ARM200F, JEOL) and spherical aberration-corrected scanning TEM (Cs-STEM, JEM-ARM200F, JEOL, operated at 80 kV) equipped with EDS that was used to analyze the nanostructures and chemical compositions. The visibility of the atomic structures was enhanced using a Fourier filter that was applied to the TEM images. The cross-sectional HR-TEM images of the MoS<sub>2</sub> samples were prepared using an FIB (JEOL). XPS (Thermo Scientific) was then carried out to examine and confirm the changes in the chemical bonding states.

**Device Fabrication and Electric Characterization:** A 300 nm thick SiO<sub>2</sub> layer was grown thermally on a highly doped p-type Si wafer as the substrate to fabricate MoS<sub>2</sub> FETs. Mo (150 nm) was deposited by radio frequency magnetron sputtering for use as the source and drain electrodes and patterned using a conventional lift-off process. Subsequently, 30 nm thick Al<sub>2</sub>O<sub>3</sub> films were fabricated by carrying out the ALD process for 300 cycles. The MoS<sub>2</sub> FET device was placed in a vacuum chamber, and electrical characterization was carried out in the dark using a parameter analyzer (Keithley 4200-SCS).

**STEM Image Observation:** All STEM images were obtained on spherical aberration-corrected scanning TEM (Cs-STEM, JEM-ARM200F) equipped with the GIF-QuantumER imaging filter (GATAN) using Gatan UltraScan 4000 4k × 4k CCD camera. The experimental results enabled the acquisition of high angle annular dark field images and fast Fourier transform (diffraction pattern), simultaneously. The minimum probe size and current for the present experiment were 0.09 nm and 23 pA, respectively. The images were taken with an operated 80 kV to limit structural damage to the MoS<sub>2</sub> monolayer sample. At this voltage and



with spherical aberration adjusted to an optimal value of  $C_s = 0.02$  mm. The convergence semi-angle was  $\approx 18$  mrad of a ronchigram flat region and an inner angle of  $45\text{--}50$  mrad. The scanning rate of each frame was typically  $6\text{ }\mu\text{s}$  per pixel and each frame consisted of  $1024 \times 1024$  pixels.

**Grain Simulation:** Selectively grown  $\text{MoS}_2$  grain structures were simulated using GIF-QuantumER imaging filter (GATAN) software. The simulated color parameters for the grain were red, green, and blue (RGB). To confirm the image simulation of the various grains in  $\text{MoS}_2$ , the three spots in the SAED pattern were selected using GATAN.

**Contact Angle Measurements:** The contact angles were measured as equilibrium static contact angle. The measuring instrument was a video-based system OCA 15EC Package 1 (DataPhysics) with the video system accuracy of  $\pm 0.1^\circ$ , employing drops of DI water with  $10\text{ }\mu\text{L}$ .

## Supporting Information

Supporting Information is available from the Wiley Online Library or from the author.

## Acknowledgements

This research was supported by the MSIT (Ministry of Science and ICT), Korea, under the ICT Consilience Creative program (IITP-2017-2017-0-01015) supervised by the IITP (Institute for Information & Communications Technology Promotion).

## Conflict of Interest

The authors declare no conflict of interest.

## Keywords

chemical vapor deposition (CVD), grains, molybdenum disulfide ( $\text{MoS}_2$ ), selective growth, super hydrophilic

Received: July 3, 2017  
Revised: August 17, 2017  
Published online:

- [1] Y.-H. Lee, Y.-H. Zhang, W. Zhang, M.-T. Chang, C.-T. Lin, K.-D. Chang, Y.-C. Yu, J. T.-W. Wang, C.-S. Chang, L.-J. Li, T.-W. Lin, *Adv. Mater.* **2012**, *24*, 2320.
- [2] S. Y. Yang, G. W. Shim, S.-B. Seo, S.-Y. Choi, *Nano Res.*, **2017**, *10*, 255.
- [3] J. Zeng, X. Yan, Z. Lu, H. Qiu, G. Xu, X. Zhou, P. Wang, X. Pan, K. Liu, L. Jiao, *Adv. Mater.* **2017**, *24*, 1604540.
- [4] C. Gong, C. Huang, J. Miller, L. Cheng, Y. Hao, Y. Cobden, J. Kim, R. S. Ruoff, R. M. Wallace, K. Cho, X. Xu, Y. J. Chabal, *ACS Nano* **2013**, *7*, 11350.
- [5] C. Muratore, J. J. Hu, B. Wang, M. A. Haque, J. E. Bultman, *Appl. Phys. Lett.* **2014**, *104*, 261604.
- [6] C. Martella, P. Melloni, E. Cinquanta, E. Cianci, M. Alia, M. Longo, A. Lamperti, S. Vangelista, M. Fanciulli, A. Molle, *Adv. Electron. Mater.*, **2016**, *2*, 1600330.
- [7] Y. Jang, S. Yeo, H.-B.-R. Lee, H. Kim, S.-H. Kim, *Appl. Surf. Sci.* **2016**, *365*, 160.
- [8] J. J. Pyeon, S. H. Kim, D. S. Jeong, S.-H. Baek, C.-Y. Kang, J.-S. Kim, S. K. Kim, *Nanoscale* **2016**, *8*, 10792.
- [9] B. Simone, K. Daria, K. Andras, *ACS Nano* **2013**, *7*, 3246.
- [10] E. Zhang, W. Wang, C. Zhang, Y. Jin, G. Zhu, Q. Sun, D. W. Zhang, P. Zhou, F. Xiu, *ACS Nano* **2015**, *9*, 612.
- [11] K. Roy, M. Padmanabhan, S. Goswami, T. P. Sai, *Nat. Nanotechnol.* **2013**, *8*, 826.
- [12] J. Wang, J.-K. Huang, C.-H. Chen, Y.-H. Chang, Y.-J. Chen, L.-J. Li, *Adv. Mater.* **2013**, *25*, 3456.
- [13] C. Chen, H. Qiao, S. Lin, C. M. Luk, Y. Liu, Z. Xu, J. Song, Y. Xue, D. Li, J. Yuan, W. Yu, C. Pan, S. P. Lau, Q. Bao, *Sci. Rep.* **2015**, *5*, 11830.
- [14] P.-L. Néstor, L. Zhong, R. P. Nihar, I.-R. Agustín, L. E. Ana, M. Amber, L. Jun, M. A. Pulickel, T. Humberto, B. Luis, *2D Mater.* **2014**, *1*, 011004.
- [15] G. He, K. Ghosh, U. Singiseti, H. Ramamoorthy, R. Somphonsane, G. Bohra, M. Matsunaga, A. Higuchi, N. Aoki, S. Najmaei, Y. Gong, X. Zhang, R. Vajtai, P. M. Ajayan, J. P. Bird, *Nano Lett.* **2015**, *15*, 5052.
- [16] M. S. Fuhrer, J. Hone, *Nat. Nanotechnol.* **2013**, *8*, 146.
- [17] J. Bai, X. Zhong, S. Jiang, Y. Huang, X. Duan, *Nat. Nanotechnol.* **2010**, *5*, 190.
- [18] K. S. Kim, Y. Zhao, H. Jang, S. Y. Lee, J. M. Kim, K. S. Kim, J.-H. Ahn, P. Kim, J.-Y. Choi, B. H. Hong, *Nature* **2009**, *457*, 706.
- [19] H. Nam, S. Wi, S. Rokni, M. Chen, M. Priessnitz, G. Lu, W. Lu, X. Liang, *ACS Nano* **2013**, *7*, 5890.
- [20] J. Zhao, H. Yu, W. Chen, R. Yang, J. Zhu, M. Liao, D. Shi, G. Zhang, *ACS Appl. Mater. Interfaces* **2016**, *8*, 16546.
- [21] N. Choudhary, J. Park, J. Y. Hwang, H.-S. Chung, K. H. Dumas, S. I. Khondaker, W. Choi, Y. Jung, *Sci. Rep.* **2016**, *6*, 25456.
- [22] Y. Xue, Y. Zhang, Y. Liu, H. Liu, J. Song, J. Sophia, J. Liu, Z. Xu, Q. Xu, Z. Wang, J. Zheng, Y. Liu, S. Li, Q. Bao, *ACS Nano* **2016**, *10*, 573.
- [23] X. Chen, Y. J. Park, T. Das, H. Jang, J.-B. Lee, J.-H. Ahn, *Nanoscale* **2016**, *8*, 15181.
- [24] Q. Yu, L. A. Jauregui, W. Wu, R. Colby, J. Tian, Z. Su, H. Cao, Z. Liu, D. Pandey, D. Wei, T. F. Chung, P. Peng, N. P. Guisinger, E. A. Stach, J. Bao, S.-S. Pei, Y. P. Chen, *Nat. Mater.* **2011**, *10*, 443.
- [25] W. Wu, Q. Yu, P. Peng, Z. Liu, J. Bao, S.-S. Pei, *Nanotechnology* **2012**, *23*, 035603.
- [26] L. Gan, H. Zhang, R. Wu, Q. Zhang, X. Ou, Y. Ding, P. Sheng, Z. Luo, *Nanoscale* **2015**, *7*, 2391.
- [27] S. N. David, Y. Zhai, A. M. van der Zande, K. O'Brien, P. Y. Huang, D. A. Chenet, J. C. Hone, X. Zhang, X. Yin, *Appl. Phys. Lett.* **2015**, *107*, 111902.
- [28] M. Ye, D. Winslow, D. Zhang, R. Pandey, Y. K. Yap, *Photonics* **2015**, *2*, 288.
- [29] M. O'Brien, N. McEvoy, D. Hanlon, T. Hallam, J. N. Coleman, G. S. Duesberg, *Sci. Rep.* **2015**, *6*, 19476.
- [30] L. Yang, X. Cui, J. Zhang, K. Wang, M. Shen, S. Zeng, S. A. Dayeh, L. Feng, B. Xiang, *Sci. Rep.* **2014**, *4*, 5649.
- [31] J. Wang, L. Chen, W. Lu, M. Zeng, L. Tan, F. Ren, C. Jiang, L. Fu, *RSC Adv.* **2015**, *5*, 4364.
- [32] M. Chhowalla, H. S. Shin, G. Eda, L.-J. Li, K. P. Loh, H. Zhang, *Nat. Chem.* **2013**, *5*, 263.
- [33] Q. H. Wang, K. Kalantar-Zadeh, A. Kis, J. N. Coleman, M. S. Strano, *Nat. Nanotechnol.* **2012**, *7*, 699.
- [34] X. Sun, C. Di, Y. Liu, *J. Mater. Chem.* **2010**, *20*, 2599.
- [35] A. M. van der Zande, P. Y. Huang, D. A. Chenet, T. C. Berkelbach, Y. You, G.-H. Lee, T. F. Heinz, D. R. Reichman, D. A. Muller, J. C. Hone, *Nat. Mater.* **2013**, *12*, 554.
- [36] Y. Gong, J. Lin, X. Wang, G. Shi, S. Lei, Z. Lin, X. Zou, G. Ye, R. Vajtai, B. I. Yakobson, H. Terrones, M. Terrones, B. K. Tay, J. Lou, S. T. Pantelides, Z. Liu, W. Zhou, P. M. A. jayan, *Nat. Mater.* **2014**, *13*, 1135.
- [37] W. Bao, N. J. Borys, C. Ko, J. Suh, W. Fan, A. Thron, Y. Zhang, A. Buyanin, J. Zhang, S. Cabrini, P. D. Ashby, A. Weber-Bergioni, S. Tongay, S. Aloni, D. F. Ogletree, J. Wu, M. B. Salmeron, P. J. Schuck, *Nat. Commun.* **2015**, *6*, 7993.
- [38] J. Hong, Z. Hu, M. Probert, K. Li, D. Lv, X. Yang, L. Gu, N. Mao, Q. Feng, L. Xie, J. Zhang, D. Wu, Z. Zhang, C. Jin, W. Ji, X. Zhang, J. Yuan, Z. Zhang, *Nat. Commun.* **2015**, *6*, 6293.